NPL
National Physical Laboratory

NPL REPORT MAT 78

FE analysis of stress and strain localisation associated with microtopographical features in corrosion pits

L. Wright, A. Turnbull

DECEMBER 2015

FE analysis of stress and strain localisation associated with microtopographical features in corrosion pits

L. Wright, A. Turnbull
Materials Division

ABSTRACT

Finite element (FE) analysis has been undertaken to quantify the distribution of stress and strain associated with corrosion pits developed experimentally in a dog-bone tensile test specimen and to compare the results with the "equivalent" smooth pit. The pits were generated in a carbon steel by an applied current using a capillary technique designed to simulate pits observed in a carbon steel pipeline in an oilfield environment. Pits in this system had the appearance of craters with protrusions and troughs at various locations in the pit. The FE modelling, undertaken for an applied stress of 96% σ_y at the pit location, indicated an increase in local strain associated with the troughs, as expected, but also strain localisation adjacent to the protrusions. In the latter case the strain exceeded yield over depths of 15 μm. These topographical features could represent potential sites for crack initiation, in which context it was notable that the density and size of these features varied from one pit to another despite a similar charging current.

Keywords: corrosion pits, stress, strain, FE analysis

ISSN 1754-2979

National Physical Laboratory
Hampton Road, Teddington, Middlesex, TW11 0LW

Approved on behalf of NPLML by Dr M Gee,
Knowledge Leader, Materials Team.

CONTENTS

1 INTRODUCTION 1
2 EXPERIMENTAL 1
3 TOPOGRAPHICAL CHARACTERISTICS OF THE PITS 2
4 FE MODEL 8
5 RESULTS 11
6 DISCUSSION 15
7 CONCLUSIONS 20
8 ACKNOWLEDGEMENTS 20
9 REFERENCES 20

1 INTRODUCTION

For many systems corrosion pits act as the precursors to stress corrosion or corrosion fatigue cracks. Remarkable progress in characterising the pit-to-crack transition has been achieved by a combination of 3D imaging by X-ray computed tomography (XCT) [1], and FE analysis of the stress and strain distribution associated with both static and growing pits in an applied stress field [2,3]. In the context of the FE analysis, the results indicated that for pits with a depth-to-width aspect ratio greater than 0.5 (hemispherical pit) the stress was a maximum near the pit mouth at low applied stresses but became a minimum near the pit mouth at stresses commensurate with the onset of plastic deformation. In essence, the reduced constraint to plastic flow near the pit mouth resulted in plastic strain being a maximum just below the pit mouth, with a redistribution of the maximum in stress away from the pit mouth. The correspondence of the maximum in plastic strain with that for crack initiation indicated by XCT is supportive of a mechanics-based explanation for the site of crack initiation. However, this analysis was conducted assuming an ideally smooth pit. In practice, a pit will tend to have significant microtopographical features reflecting the impact on corrosion activity of local variation in material microchemistry, microstructure, inclusions and constituent particles. Thus, Burns and Gangloff [4] argued that such microtopographical features were inherent in pits associated with constituent particles in aluminium alloys and the primary site for crack initiation. Ma et al. [5] also highlighted the importance of local geometric features with respect to elongated inclusions in carbon steel.

Microtopographical features will always be present in real pits. The question posed is the significance in relation to stable crack propagation. Conceptually, it could be envisaged that the length scale over which these features influenced the stress and strain distribution could be quite small; thence, embryonic cracks could conceivably arrest after a short propagation distance as the mechanical driving force decreases. Thus, crack initiation could indeed be favoured by such features but stable crack propagation could depend more critically on the macro-stresses developed around the pit. To provide insight, we have undertaken FE analysis to explore the impact of irregular geometric features on the stress/strain localisation in a pit and to assess the length scale over which stress/strain localisation extends. The modelling is focused on corrosion pits in carbon steel in a simulated oilfield environment as part of a BP sponsored project with the Massachusetts Institute of Technology (MIT) and the University of Manchester (UoM) to characterise the relationship between environment, microstructure and stress on precursors to crack initiation.

2 EXPERIMENTAL

The material tested was a X65 steel with mechanical properties as determined by MIT [6]. The material exhibited a yield point with the elastic modulus estimated as 200 GPa, and a yield stress of about 500 MPa. A plot of the stress vs plastic strain is shown in Figure 1, together with the fitted data used as input to the FE model. The grain size of the material varied from less than 0.6 µm (21% of grains) to almost 50 µm, with about 70% of grains having a size less than 4 µm [7].

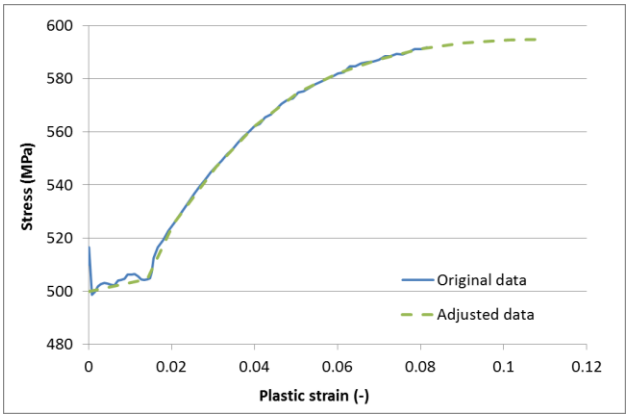

Figure 1: Stress-plastic strain relationship for X65 steel modelled showing adjusted data used as input to the FE model [from Reference 6].

The corrosion pits simulated were produced artificially and for corrosion fatigue tests would be located at the centre of dog-bone specimens (Figure 2).

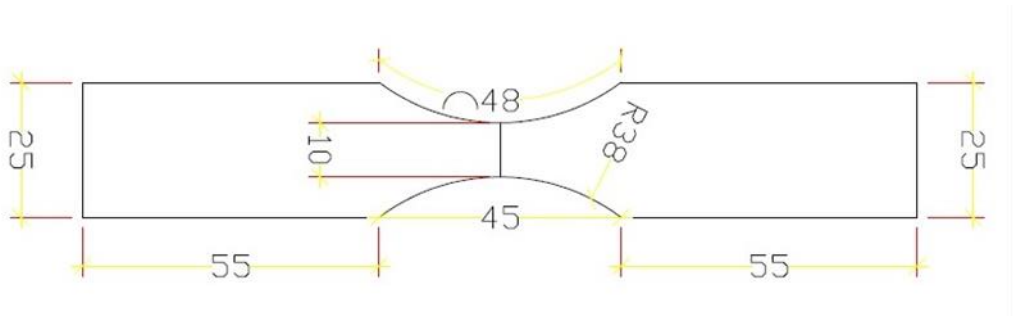

Figure 2: Dimensions of flat dog-bone specimens; specimen thickness 1.5 mm.

The pits were produced by an electrochemical capillary method at UoM [7]. The solution was 3.5% NaCl and the applied current was 0.6 mA with pits of different size produced by varying the time. The method adopted produced a pit shape that was broadly comparable with pits observed in service, from two separate pipes (Figure 3), insofar as the pit was crater-like (in contrast to the bulbous-shaped pits on stainless steel for example). The service pits showed variability and more elongation and a gradient in average depth induced by fluid flow. In addition, the local variation in service pit topography tended to be more significant (cf Figures 4-7 for pits generated in the laboratory). Nevertheless, since the laboratory generated pits would form the basis of corrosion fatigue testing, the focus of the FE analysis was on characterisation of the laboratory produced pits. Upon cleaning of the specimens a detailed 3D digital representation of the pit dimensions and geometry was generated by confocal scanning microscopy.

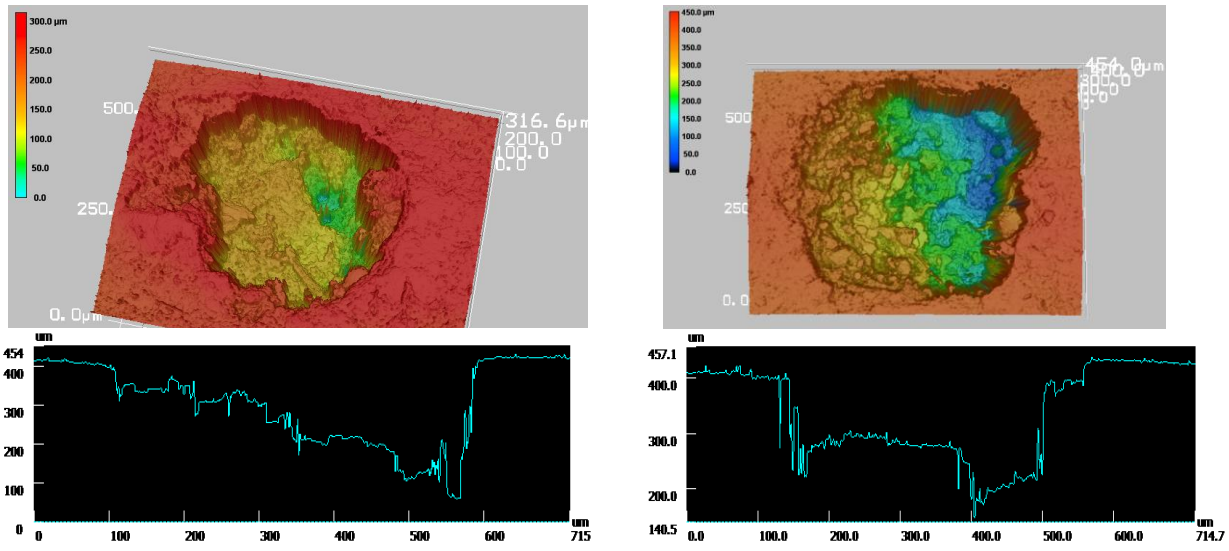

Figure 3: Image and cross-sectional profile (deepest point) for pits from two separate service pipes; scale in µm [7].

3 TOPOGRAPHICAL CHARACTERISTICS OF THE PITS

Four pits were generated by UoM using the capillary method. The full images as supplied are shown in Figures 4 to 7, and the dimensions and resolution of the supplied images are shown in Table 1. In the table, "width" refers to the x direction in Figures 4 to 7, "height" is the y direction, and "depth" is the z direction.

The table shows that the images of pits 1800s and 3600s have higher resolution over a smaller volume than the images of pits P200 and P275.

Table 1: Image names, size of imaged region, and resolution of surface image.

Image name	Image width (mm)	Image height (mm)	Image depth (mm)	Image resolution (mm)
P200	2.00	2.00	0.25	0.022
P275	2.00	2.00	0.28	0.017
1800s	0.715	0.534	0.232	0.005
3600s	0.708	0.985	0.162	0.005

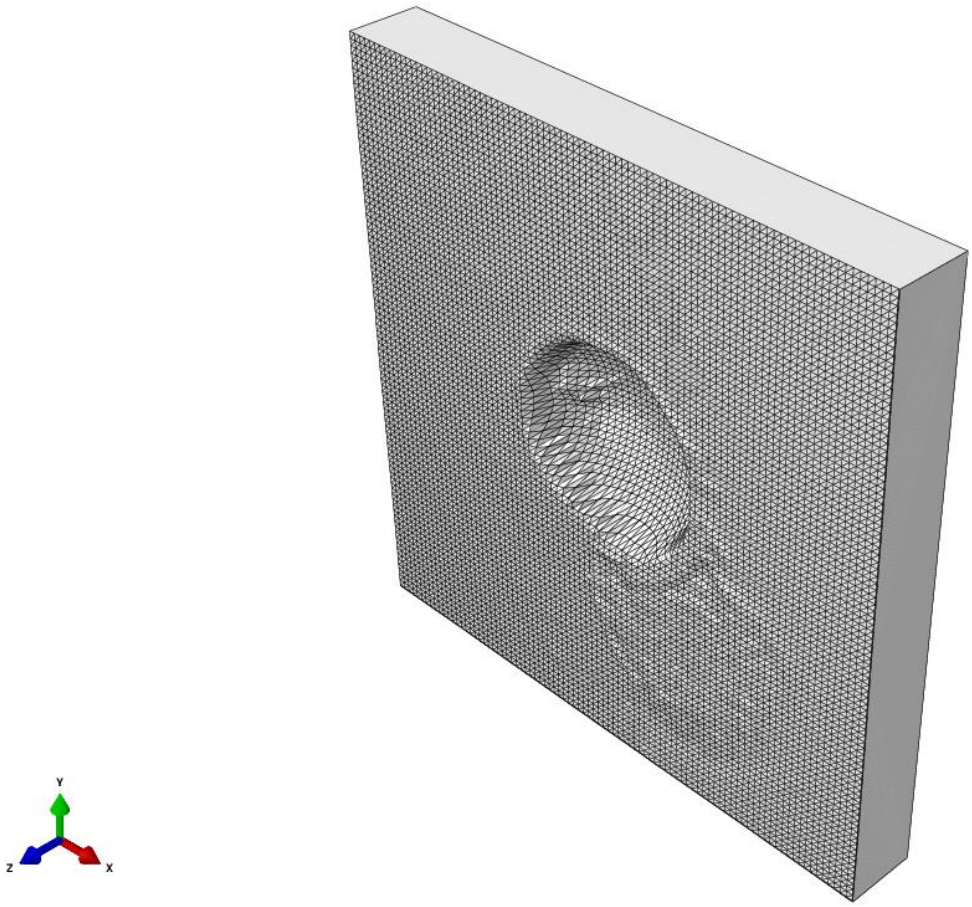

Figure 4: Full image of pit labelled P200 as supplied.

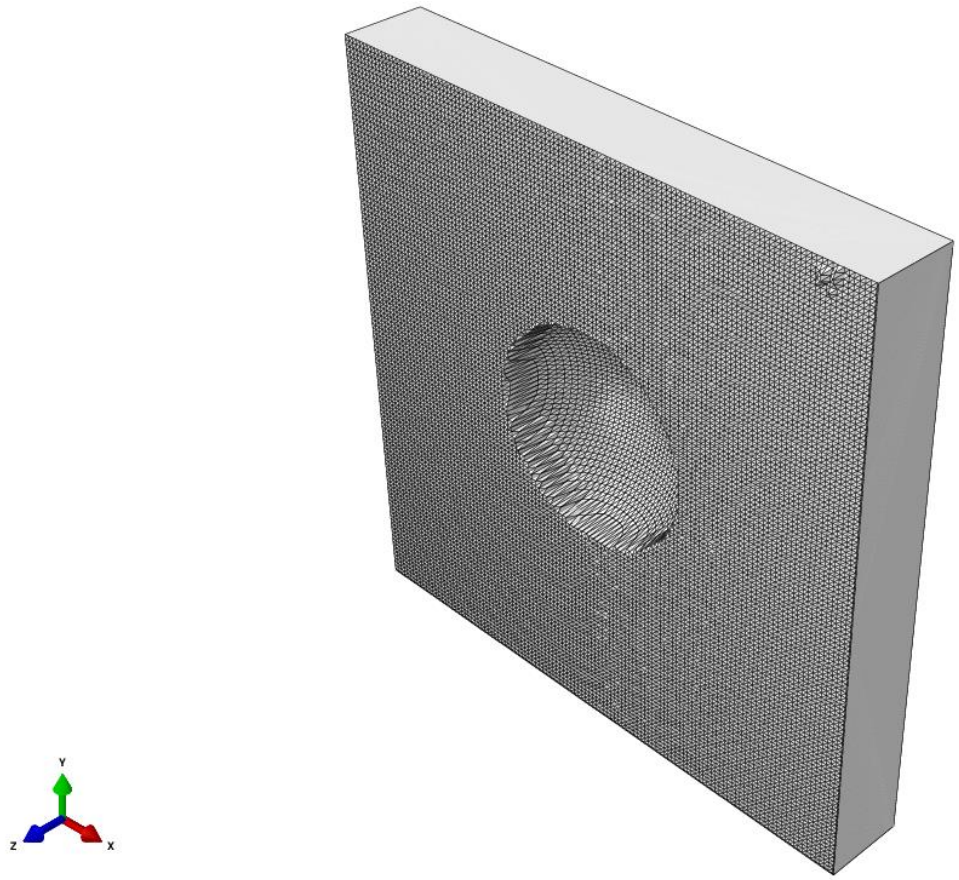

Figure 5: Full image of pit labelled P275 as supplied.

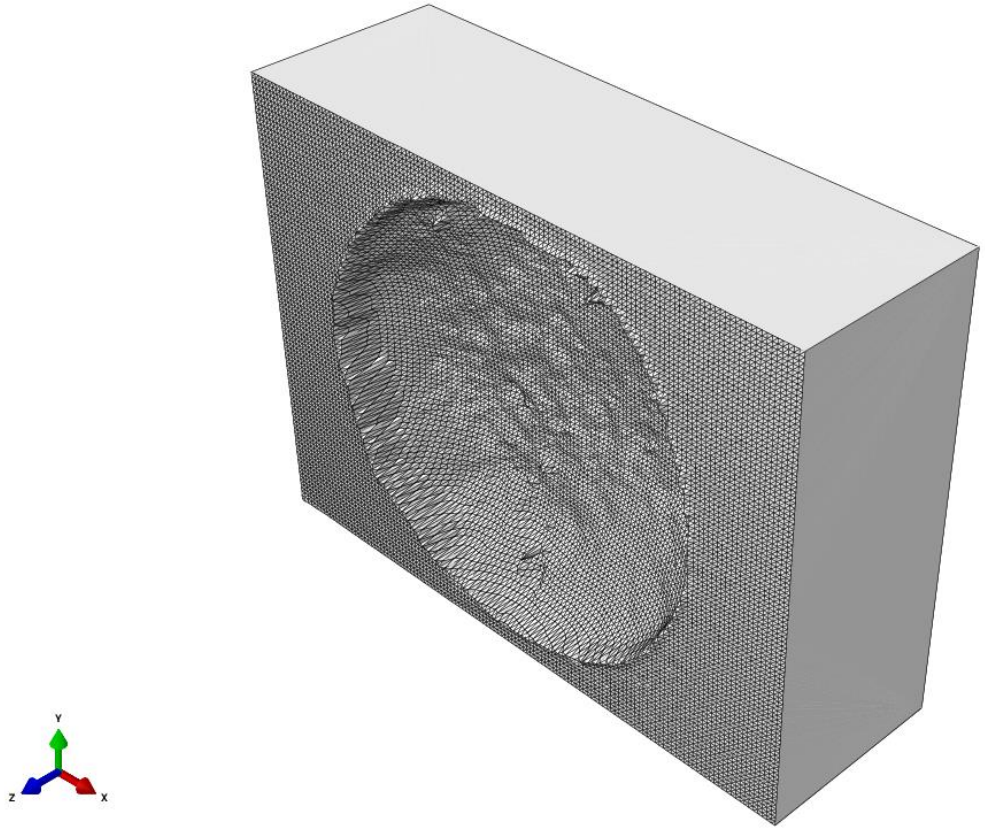

Figure 6: Full image of pit labelled 1800s as supplied.

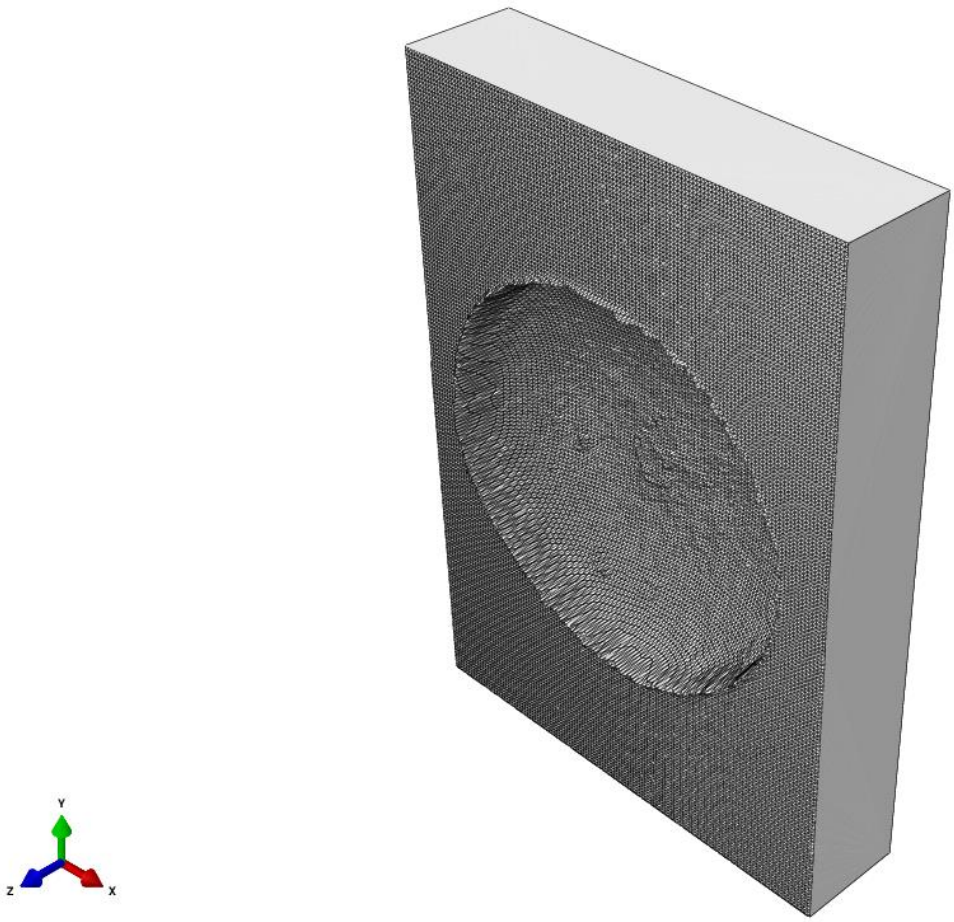

Figure 7: Full image of pit labelled 3600s as supplied.

The meshed images of the laboratory grown pits, shown in Figures 8 to 111, indicate the degree of roughness of the pit. No attempt was made to characterise the roughness numerically. Inspection of these images suggests that:

- the pit labelled P200 is smooth other than a single protrusion on the left of the image in Figure 8 and a slightly raised region near the centre of the image (both circled in red);
- the pit labelled P275 is almost completely smooth and has no obvious protrusions, but some roughness is present at the pit mouth due to the steepness of the sides;
- the pit labelled 1800s is generally not smooth and has several protrusions (circled in red) and some troughs (circled in blue);
- the pit labelled 3600s has a rough surface, one large protrusion (circled in red) and a number of smaller ridges.

It is apparent that the real pits generated for corrosion fatigue testing by the particular capillary method show an intrinsic variability in local topography within a single pit but also with differences from one specimen to another under the same nominal testing conditions. If such specimen-to-specimen topographical variation were to impact on the pit-to-crack transition then significant variability in results from laboratory testing under controlled conditions could arise if these local stresses and strains were to lead to stable propagating cracks.

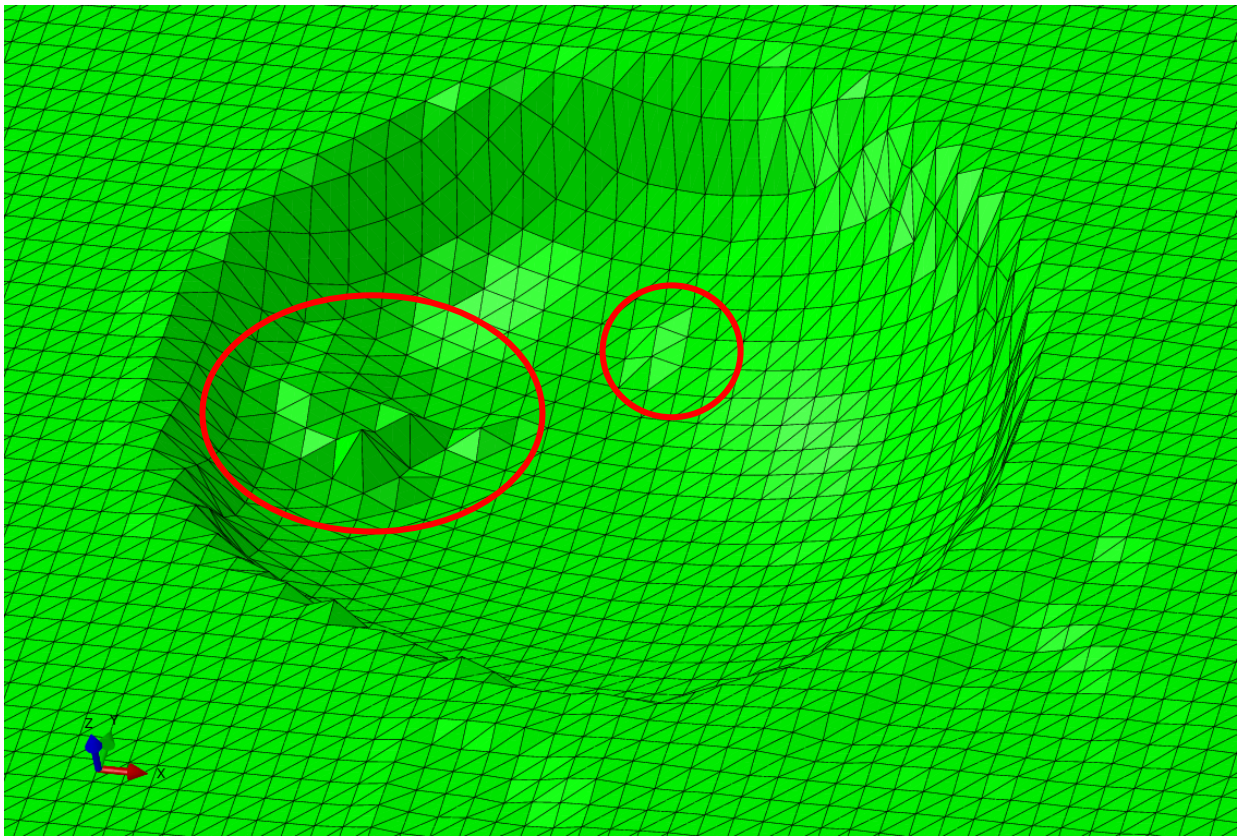

Figure 8: Image of pit labelled P200. Raised regions are circled in red.

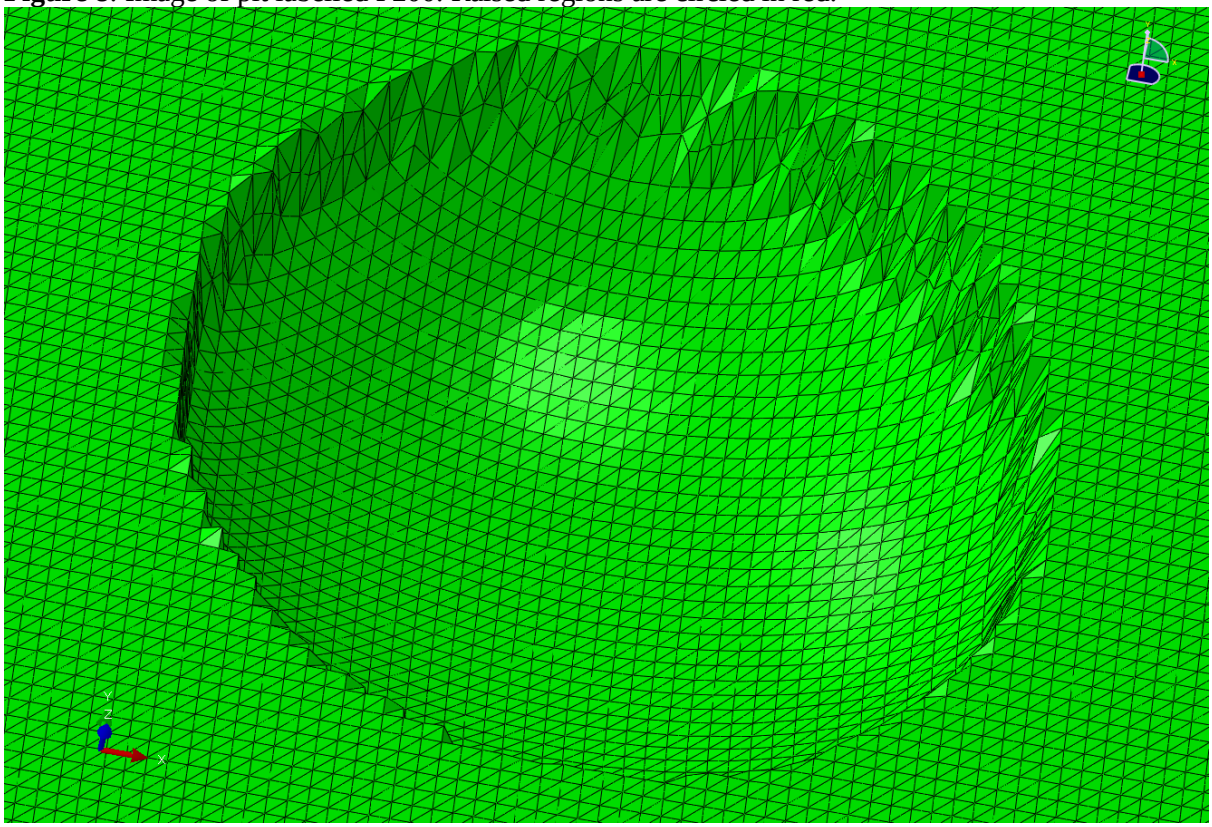

Figure 9: Image of pit labelled P275

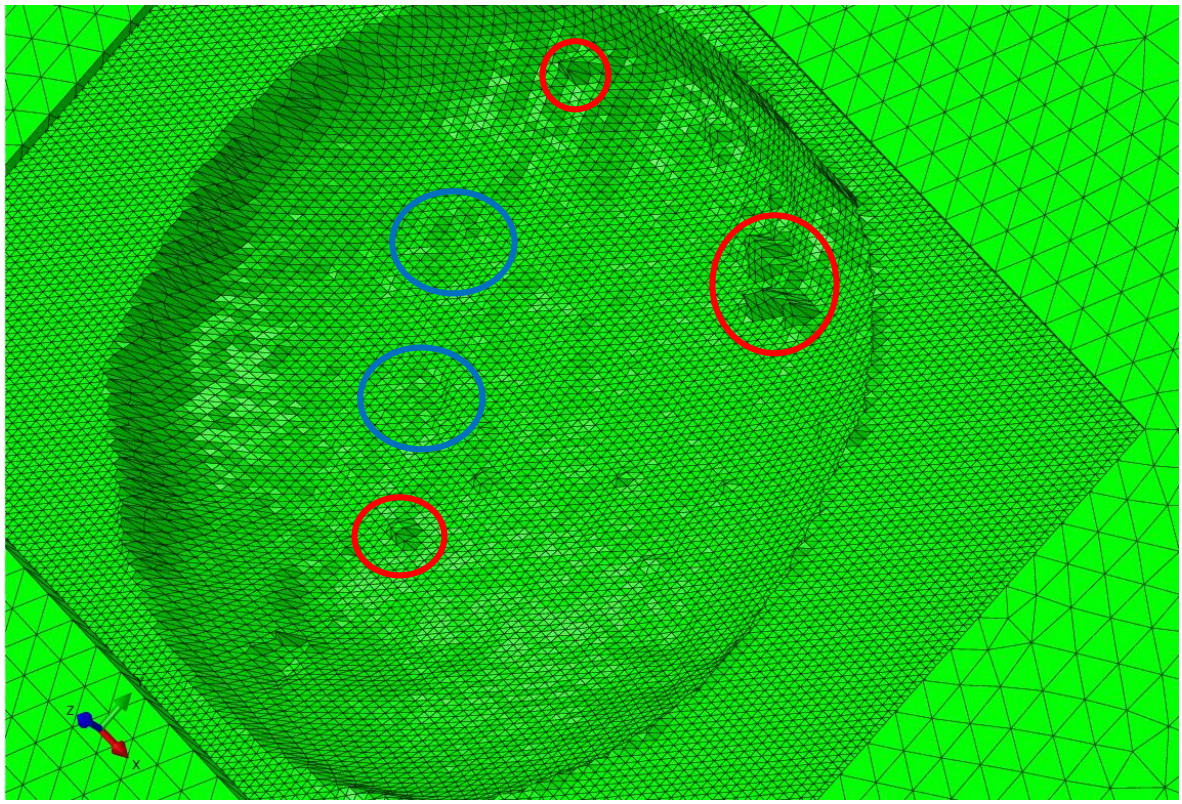

Figure 10: Image of pit labelled 1800s. Raised regions are circled in red, lowered trough-like regions are circled in blue.

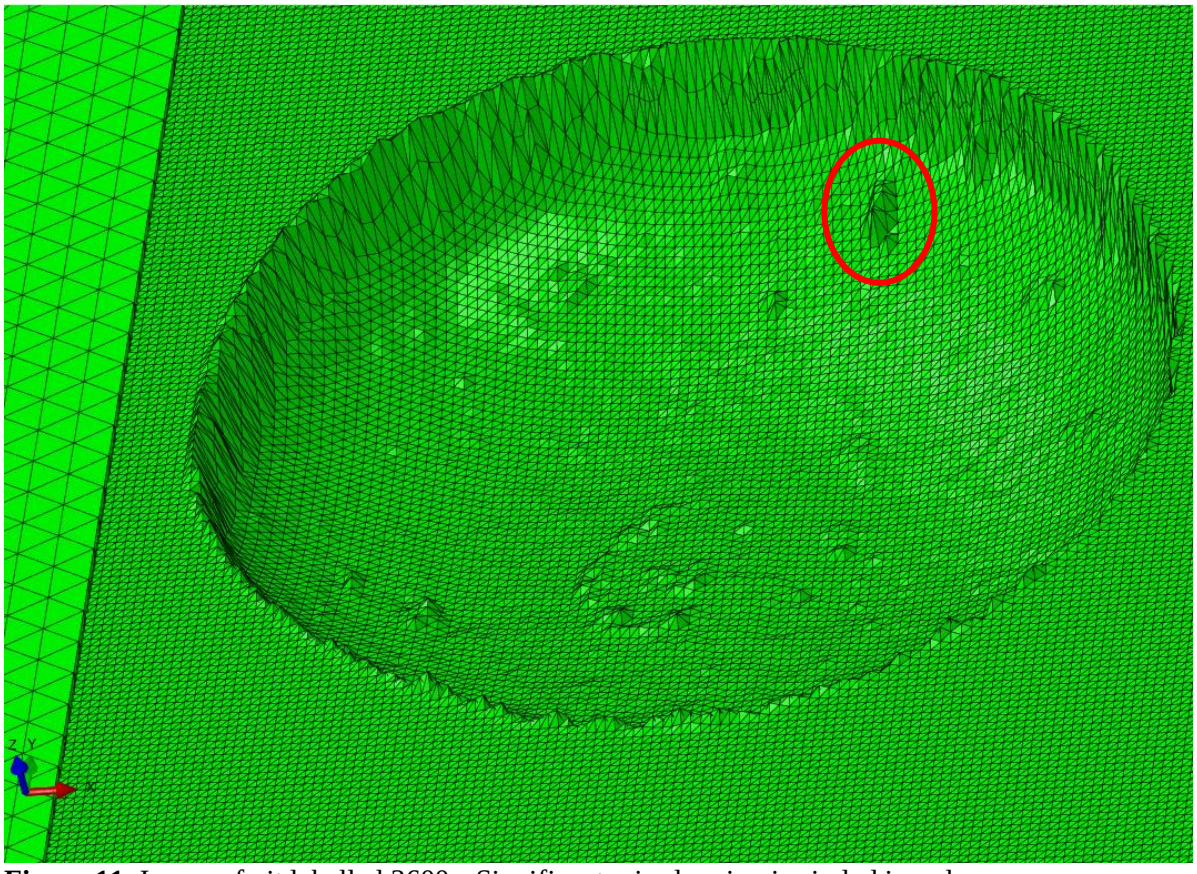

Figure 11: Image of pit labelled 3600s. Significant raised region is circled in red.

4 FE MODEL

Modelling of the stress and strain distribution around the pit was undertaken using the actual pit geometry, supplied as STEP files, or using a smoothed version of the first type, designed, by comparison, to isolate the contribution of microtopographical features. An example of the smoothing is shown in Figure 12 (only the cross-section of the pit is shown), in which a continuous smooth line (an ellipse) has been fitted to the cross-section.

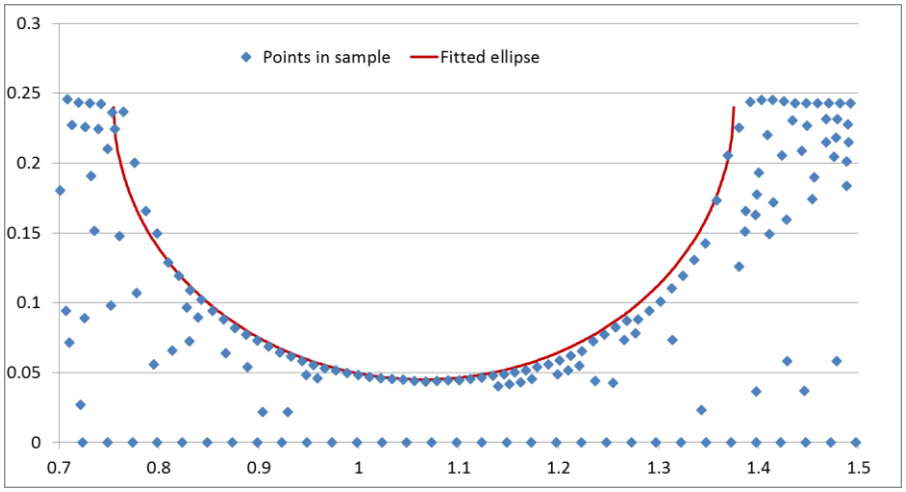

Figure 11: Cross-section through a pit and fitted ellipse (data shown is taken from image P200).

All pits were well approximated by ellipsoids similar to that produced by rotation of the curve shown in Figure 12 around a vertical axis. Table 2 lists the pit names and the geometric parameters defining the fitted curves.

Table 2: Pit names and fitted parameters defining the smoothed geometry.

Pit name	Pit depth (mm)	Pit radius (mm)
P200	0.20	0.31
P275	0.28	0.36
1800s	0.11	0.35
3600s	0.14	0.29

In modelling the dog-bone specimen, a longitudinal load of 7.6 kN was applied throughout, via displacement control (0.2 mm displacement at end of specimen) to improve convergence, such that the maximum stress in the gauge length where the pit would be positioned would be 480 MPa in the absence of the pit (cf. yield strength of 500 MPa). The maximum stress is actually in the curved section of the gauge length and would exceed yield. A value of Poisson's ratio of 0.3 was adopted.

Comparison of a full tensile test specimen with a typically sized pit and a full tensile test specimen without a pit shows that the stress distribution is only altered by the pit within a comparatively small volume. This is shown in Figures 13 and 14, where tensile specimens with and without a pit are compared using the same stress scale. The highly localised effect of the pit means that a sub-model of just the region immediately surrounding the pit can be created as a more computationally efficient alternative to a model of the full tensile specimen.

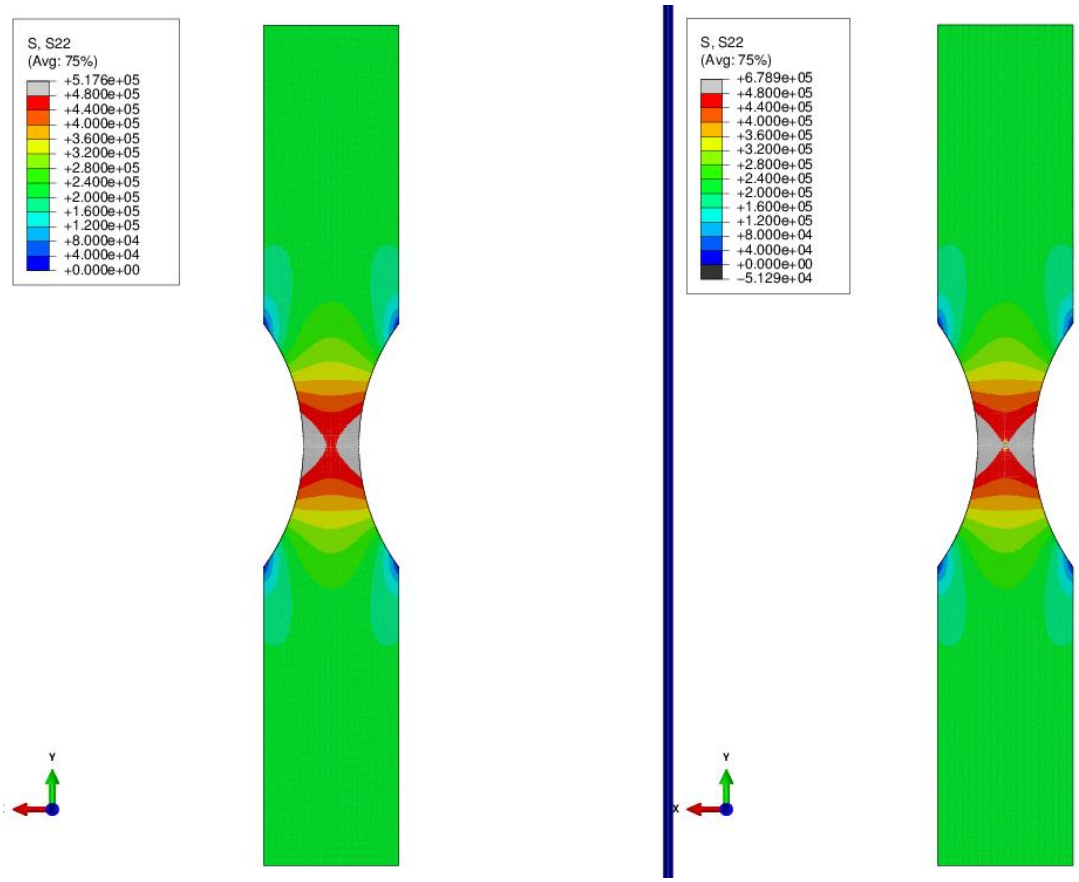

Figure 13: Longitudinal stress in full tensile specimens with (right hand image) and without (left hand image) a pit. Units are kPa.

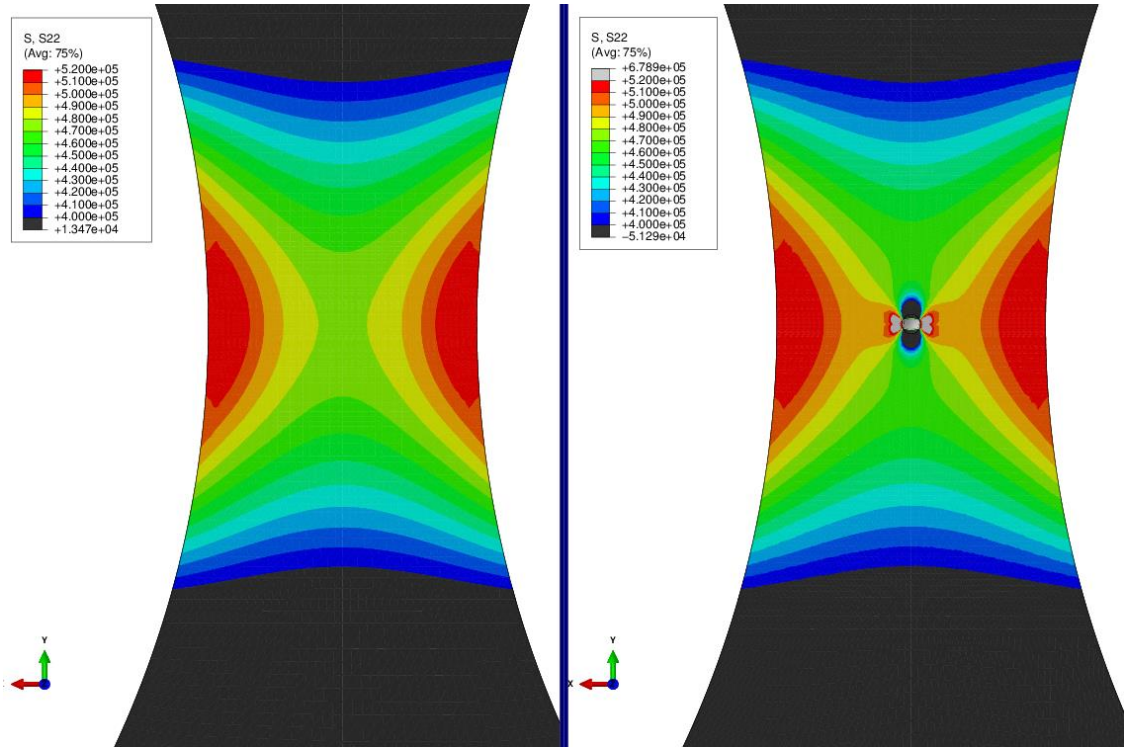

Figure 14: Close-up of Figure 13 showing the region immediately around the pit. Colour scales are identical and have been adjusted to highlight regions of difference between the two sets of results. Units are kPa

Analysis of these results showed that the computed stresses on the edges of a volume centred on the pit measuring 5 mm by 10 mm by 1.5 mm (i.e. the full sample thickness) agreed sufficiently well (better than 0.015% for tensile stress). Thus, the pit could be regarded as having no effect outside of that volume. Abaqus, the simulation package used for this work, has a sub-modelling capability that allows the user to use the results of one model to define the boundary conditions of a more detailed model of a part of the geometry. Hence, the full model of the tensile specimen with no pit could be used to define the displacement boundary conditions on the edges of a 5 mm by 10 mm by 1.5 mm model, which would include the details of each pit. This improved the computational efficiency of the modelling process.

However, as noted above, the most detailed pit images had a feature resolution of approximately 5 µm within a volume measuring approximately 0.7 mm by 0.5 mm by 0.225 mm, which is much smaller than the sub-model volume; hence, it was necessary to embed the models created from the detailed pit images within the larger volume. The geometries could not be merged directly because the pit image has surface roughness features that cannot easily be merged into a larger volume.

This embedding was done by creating a volume with a hole the same size as the pit image and defining tie constraints between the edges of the pit volume and the hole. The tie constraints ensure continuity of displacement across two faces. Continuity of forces is enforced overall, but a large difference in mesh density across the two faces can lead to unwanted stress effects. An example of the effects of stress localisation is shown in Figure 15. The longitudinal stress contours are discontinuous and show local maxima where the detailed mesh of the pit image meets the coarser mesh of the main volume. This effect was reduced by using a more refined mesh where the two volumes met.

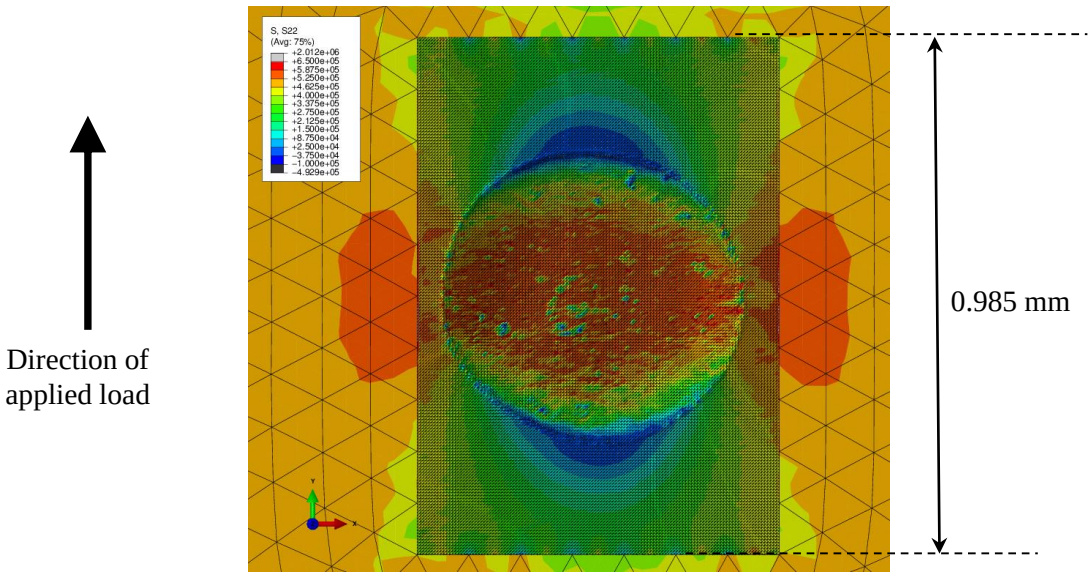

Figure 15: Example of stress localisation for real pit. Note high mesh density for pit and local region around pit and coarser mesh at greater distance. Units are kPa

A further complication was caused by the surface mismatch at the meeting between the two surfaces. If the detailed region sits above the surface of the coarse mesh, then the top surface of the detailed region is not tied to the coarse mesh and so the stress in the detailed region is lower than it should be. This phenomenon is illustrated in Figure 16. The upper picture shows a close-up of a line of stress discontinuity, and the lower picture shows a partial section through the sample that shows that the stress is reduced at the surface because the surface node is not constrained by the main sample.

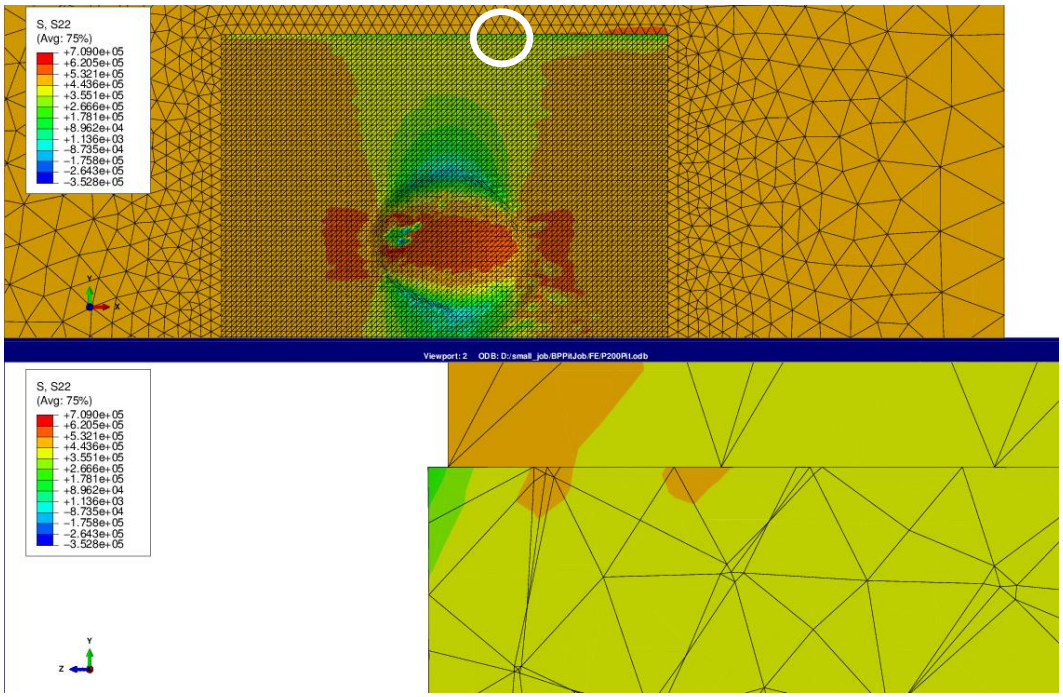

Figure 16: Example of stress relaxation at the surface. Note that the lower image has had a change of orientation and a section applied. Approximate location of lower image is circled on upper image. Units are kPa

In practice, there would be no stress relaxation because the surface would be continuous. Hence efforts were made to ensure that all nodes in the detailed region lay below the surface of the main volume so that their motion would be controlled by that of the main volume. The corollary of this was that the surface of the main volume underwent some stress relaxation, but since the region of interest is the detailed region it is more important that the load is transferred to this region than it is that the stress at the surface of the main volume is correct (although the two will, to some degree, be linked).

The embedding approach was not necessary for the smoothed pit models because the smoothed pit sample geometries can be created directly by removing the pit volume from a cuboidal sample.

5 RESULTS

Figures 17 to 224 show direct comparison of the longitudinal stress and longitudinal plastic strain results of the real pits (right hand image in each plot) and the idealised smooth pit equivalent (left hand image in each plot). Each pair of images is plotted using the same colour scale so that direct comparison is possible. It should be noted that there are some discrepancies in stress at the interface between the detailed pit region and the large domain in the results of the models with the real pits. These discrepancies have occurred because it has not been possible to join perfectly the rough surface of the pit image with the smooth surface of the rest of the domain, so the pit image has been inserted slightly below the surface of the domain to ensure that the full load is transferred to the pit. As a result of this insertion, there is some evidence of stress relief at the surface of the main domain, but the pit experiences the correct tensile load.

The stress results show some regions of compressive stress at the pit mouth, albeit relative small. Modelling of a vertical through-thickness hole also showed a similar region of compression.[1]

1. Such a compressive stress is to be expected as noted elsewhere; http://www.fracturemechanics.org/fm/hole.html

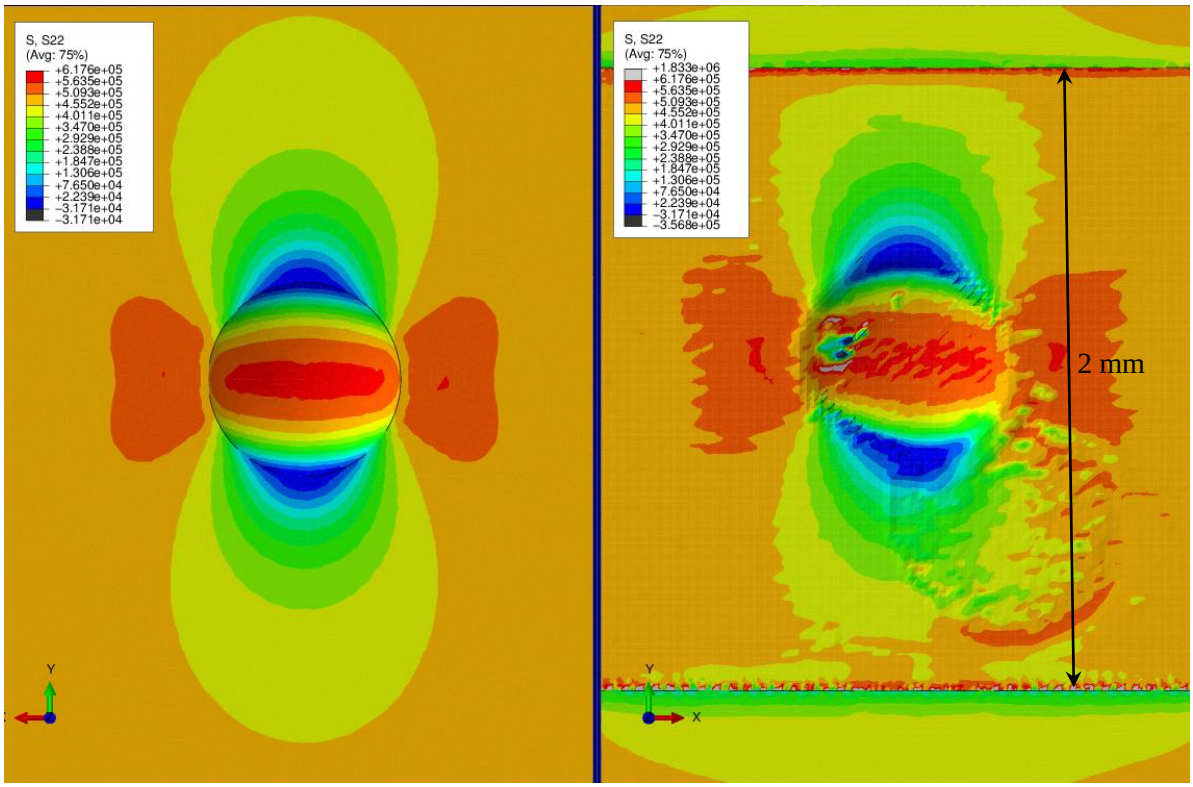

Figure 17: Longitudinal stress in the pit labelled P200. Left-hand plot is the idealised model, right-hand plot is the real pit image. Units are kPa. Direction of loading is top-to-bottom of the page.

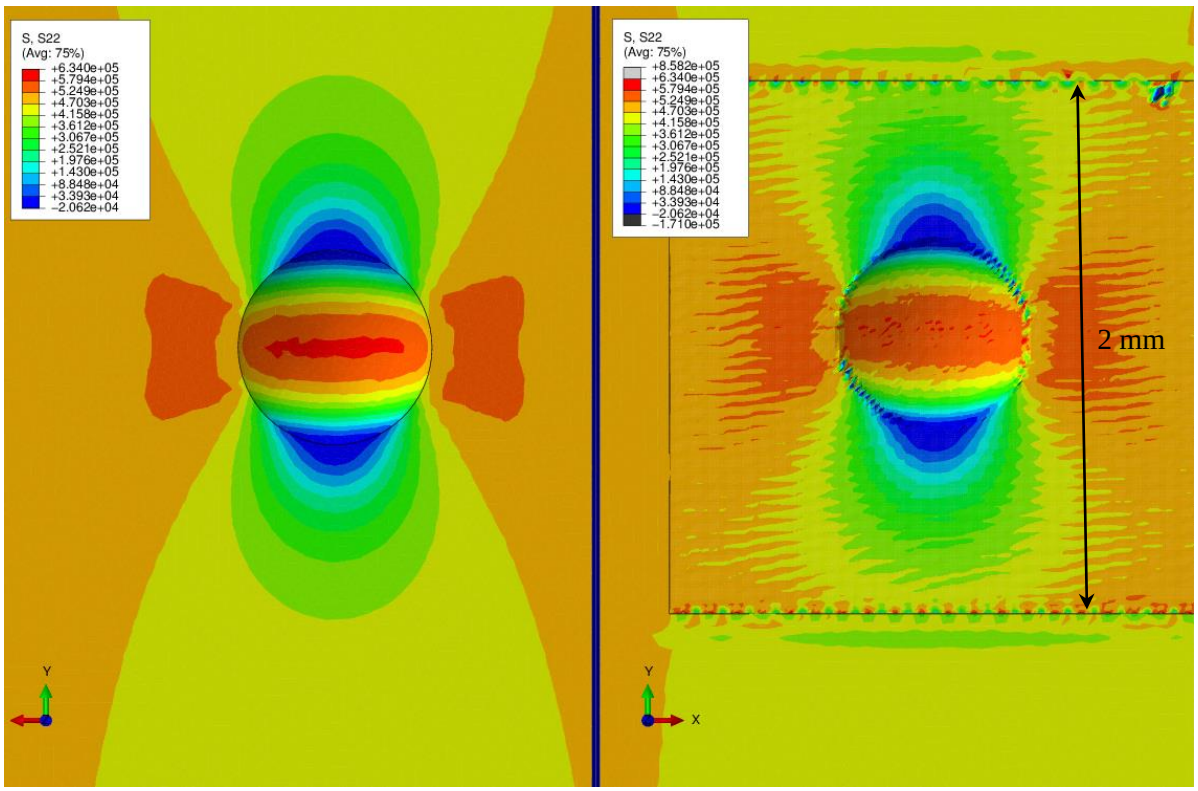

Figure 18: Longitudinal stress in the pit labelled P275. Left-hand plot is the idealised model, right-hand plot is the real pit image. Units are kPa. Direction of loading is top-to-bottom of the page.

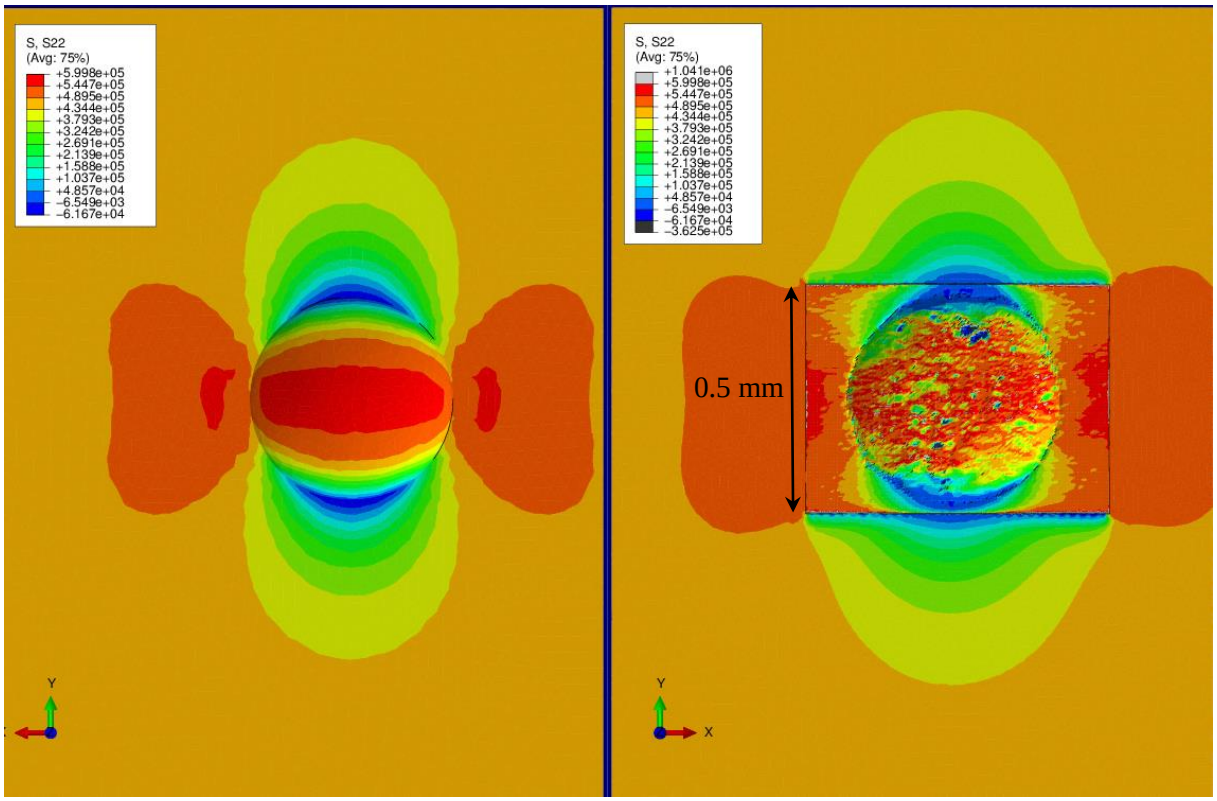

Figure 19: Longitudinal stress in the pit labelled 1800s. Left-hand plot is the idealised model, right-hand plot is the real pit image. Units are kPa. Direction of loading is top-to-bottom of the page.

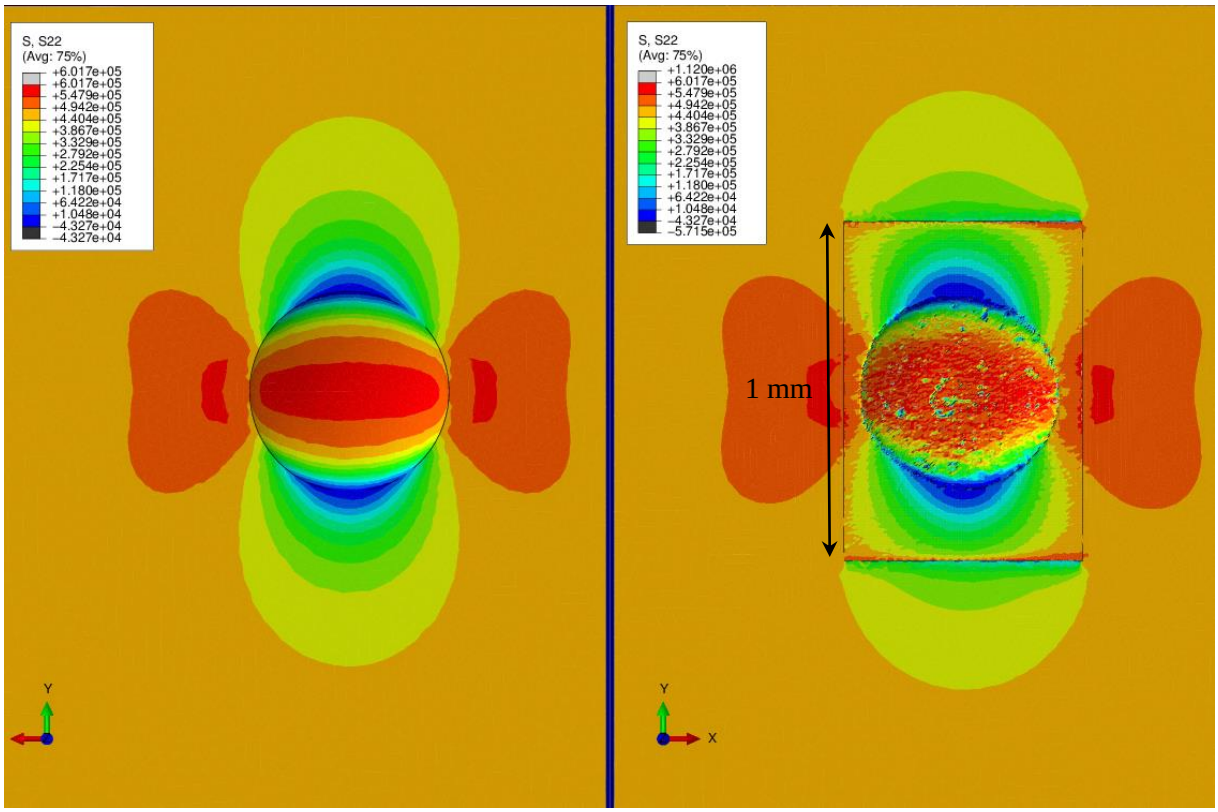

Figure 20: Longitudinal stress in the pit labelled 3600s. Left-hand plot is the idealised model, right-hand plot is the real pit image. Units are kPa. Direction of loading is top-to-bottom of the page.

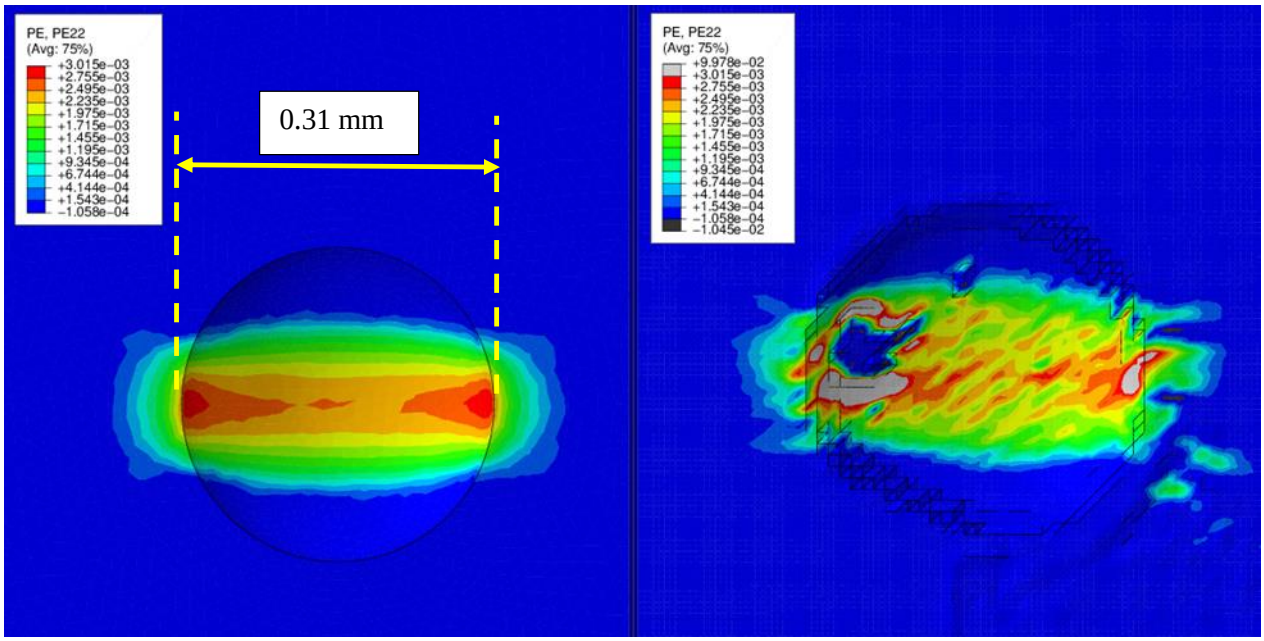

Figure 21: Longitudinal plastic strain in the pit labelled P200. Left-hand plot is the idealised model, right-hand plot is the real pit image. Direction of loading is top-to-bottom of the page.

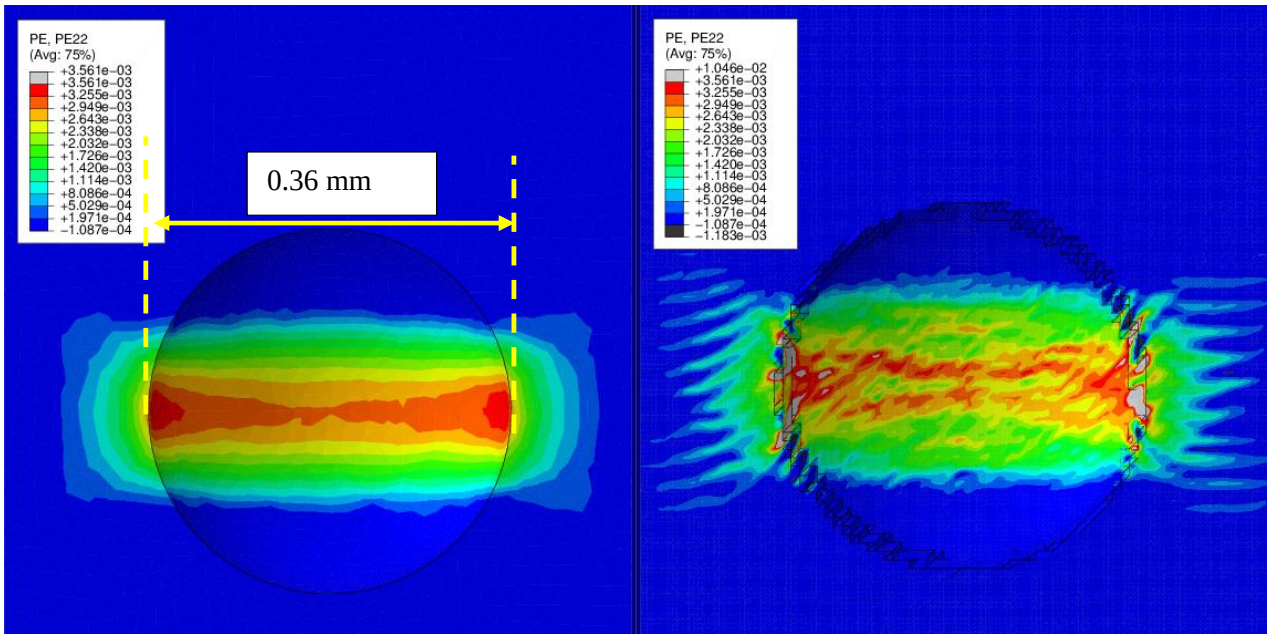

Figure 22: Longitudinal plastic strain in the pit labelled P275. Left-hand plot is the idealised model, right-hand plot is the real pit image. Direction of loading is top-to-bottom of the page.

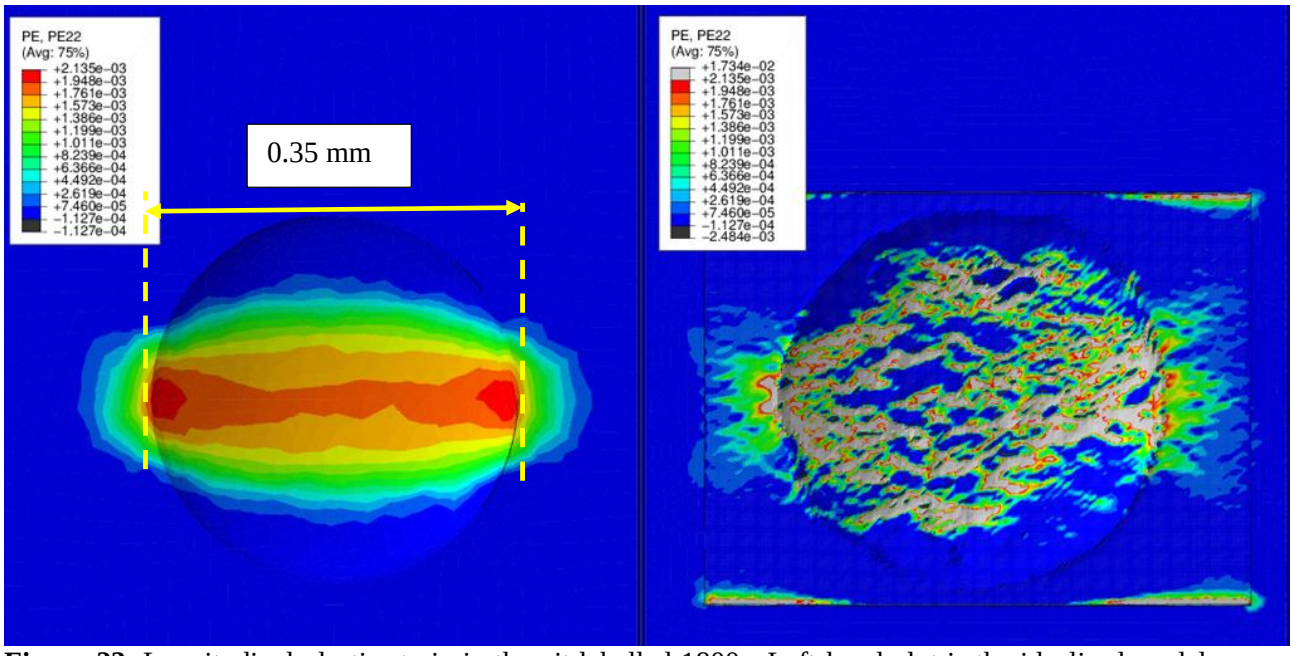

Figure 23: Longitudinal plastic strain in the pit labelled 1800s. Left-hand plot is the idealised model, right-hand plot is the real pit image. Direction of loading is top-to-bottom of the page.

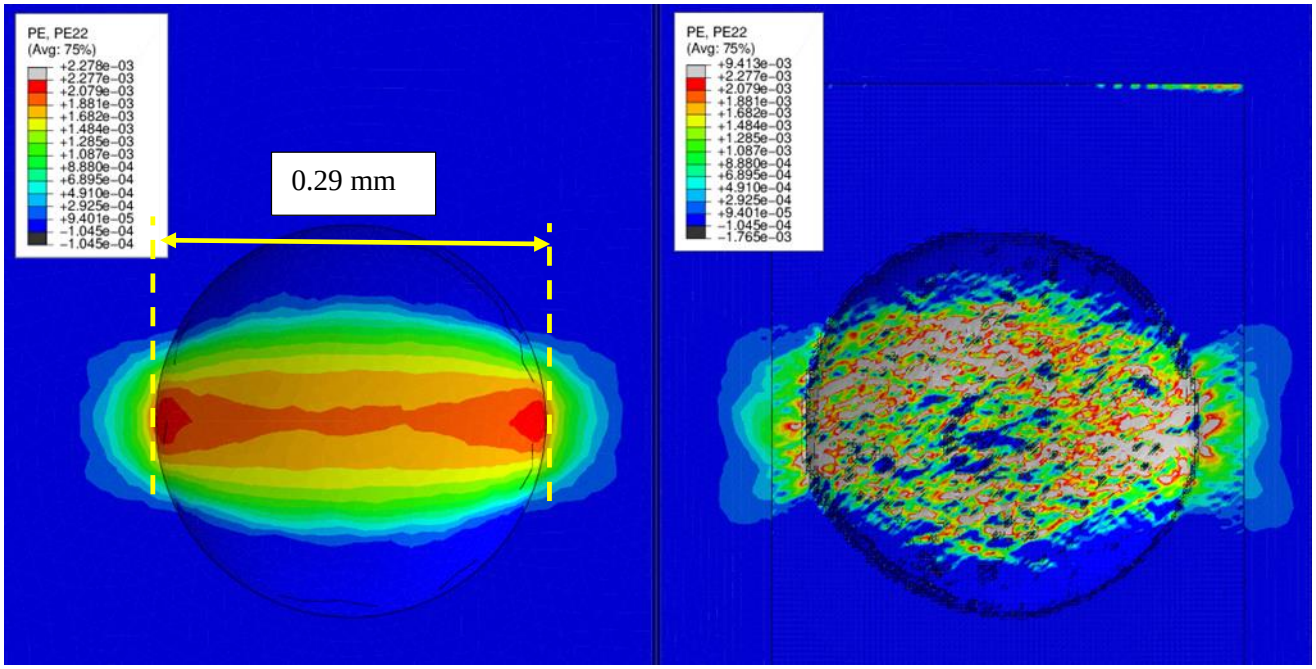

Figure 24: Longitudinal plastic strain in the pit labelled 3600s. Left-hand plot is the idealised model, right-hand plot is the real pit image. Direction of loading is top-to-bottom of the page. Extra black lines in the left-hand plot are imaging artefacts caused by the FE software and should be ignored.

6 DISCUSSION

Regarding the smooth pits only first, it will be noted that the stress is a maximum at the base of the pit, while the plastic strain is a maximum close to the pit mouth, for which there is reduced constraint to deformation. This is similar to the behaviour observed previously for hemispherical pits and for pits with a larger aspect ratio.

A surprising feature in relation to the stress distribution and the stress "wings" on either side of the pit is the dip in stress immediately at the pit mouth but on the external surface. This is most discernible in Figures 17 and 18, with Figures 19 and 20 showing a peak in stress a short distance from the pit mouth. This behaviour seems likely associated with the steepness of the pit walls though a conceptual explanation is not readily apparent.

Figures 17 and 18 and 21 and 22 show that the stress and strain distributions in the idealised (smoothed) and actual pits are broadly similar for pits labelled P200 and P275 with the exception of the stress/strain localisation around the two protrusions that were circled in Figure 4. The distribution around the larger protrusion is shown in close up in Figure 25.

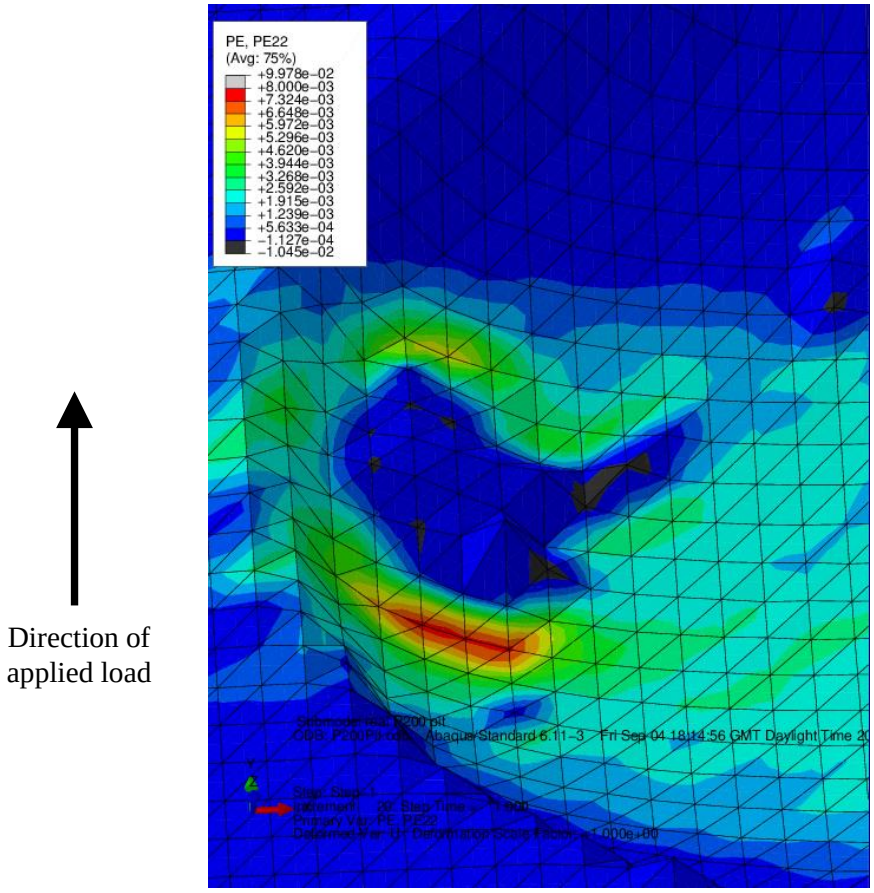

Figure 25: Region of elevated strain close to large protrusion in pit labelled P200.

There is also some disagreement in strain values at the mouth of the pit between smoothed and real pit images in Figures 21 and 22 which cannot be attributed to topography. This may be due to the mesh not being adequate: the mesh generated simply from the pit images may need refinement to accurately predict strain localisation for a pit with steep sides.

Figures 19 and 20 and 23 and 24 show marked deviation between the stress and strain distributions for the smoothed pits compared to the real pits (labelled 1800 and 3600). The influence of local geometric features is much more marked with significant local enhancement of stress and strain. As was noted above, levels of strain are low in areas of protrusion and high at the "foot" of protrusions, presumably because of some shielding effect. An example of this phenomenon for the pit labelled 1800s is shown in Figure 26. This figure shows the double protrusion circled in red in Figure 10 in close-up.

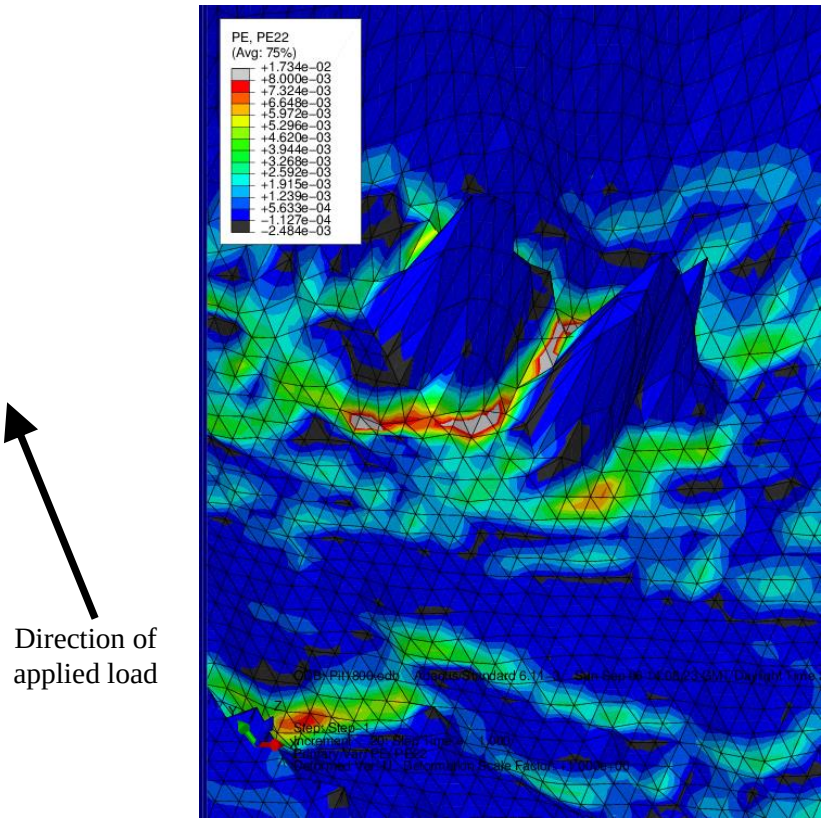

Figure 26: High strain in regions of pit features for pit labelled 1800s.

Further examination of the strain distribution in the pit labelled 1800s (Figure 27) shows that the trough-like regions have a high level of strain, as might be anticipated. Figures 28 and 29 show a cross-section through the unsmoothed (Figure 28) and smoothed (Figure 29) versions of P1800s. The geometric point in Figure 28 is part of the topological feature in Figure 26. These figures show that surface roughness causes plastic strain below the surface of the pit.

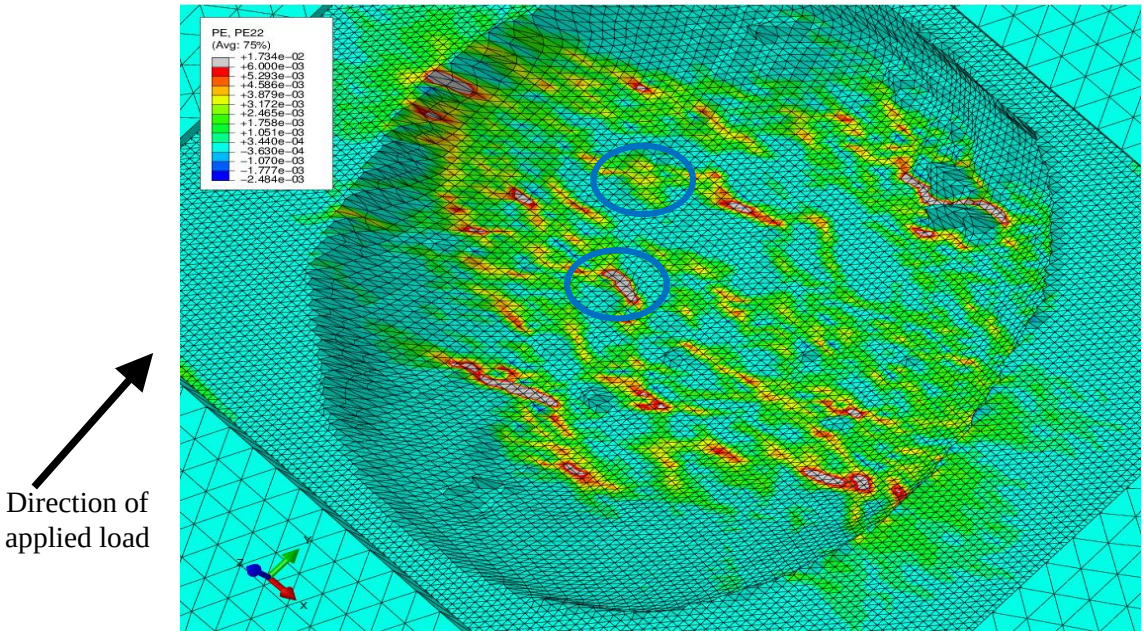

Figure 27: Strain distribution around the trough-like regions in the pit labelled 1800s. Colour scale has been adjusted so that the troughs are visible. As in Figure 6, they are circled in blue.

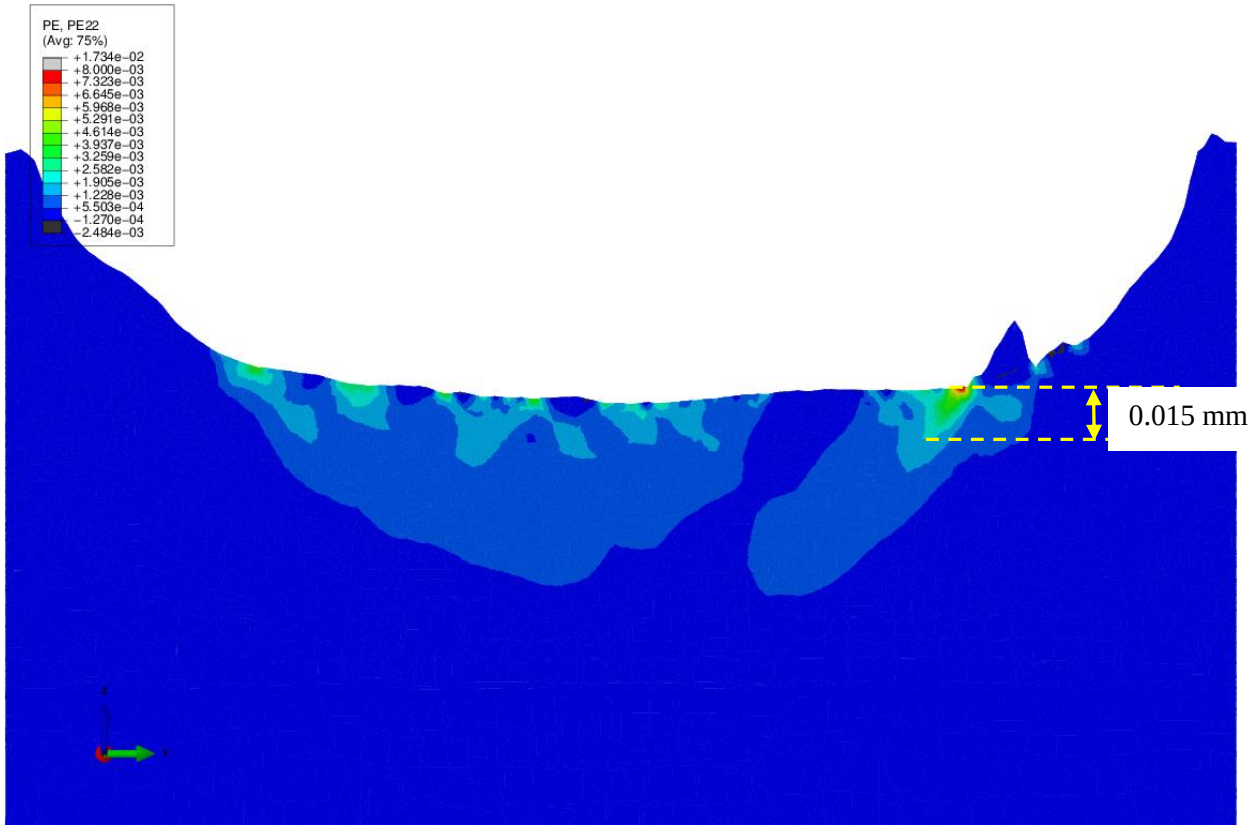

Figure 28: Cross-section of the pit labelled 1800s, showing localised plastic strain caused by surface roughness. The direction of loading is left to right. Note the change in colour coding from Figure 23

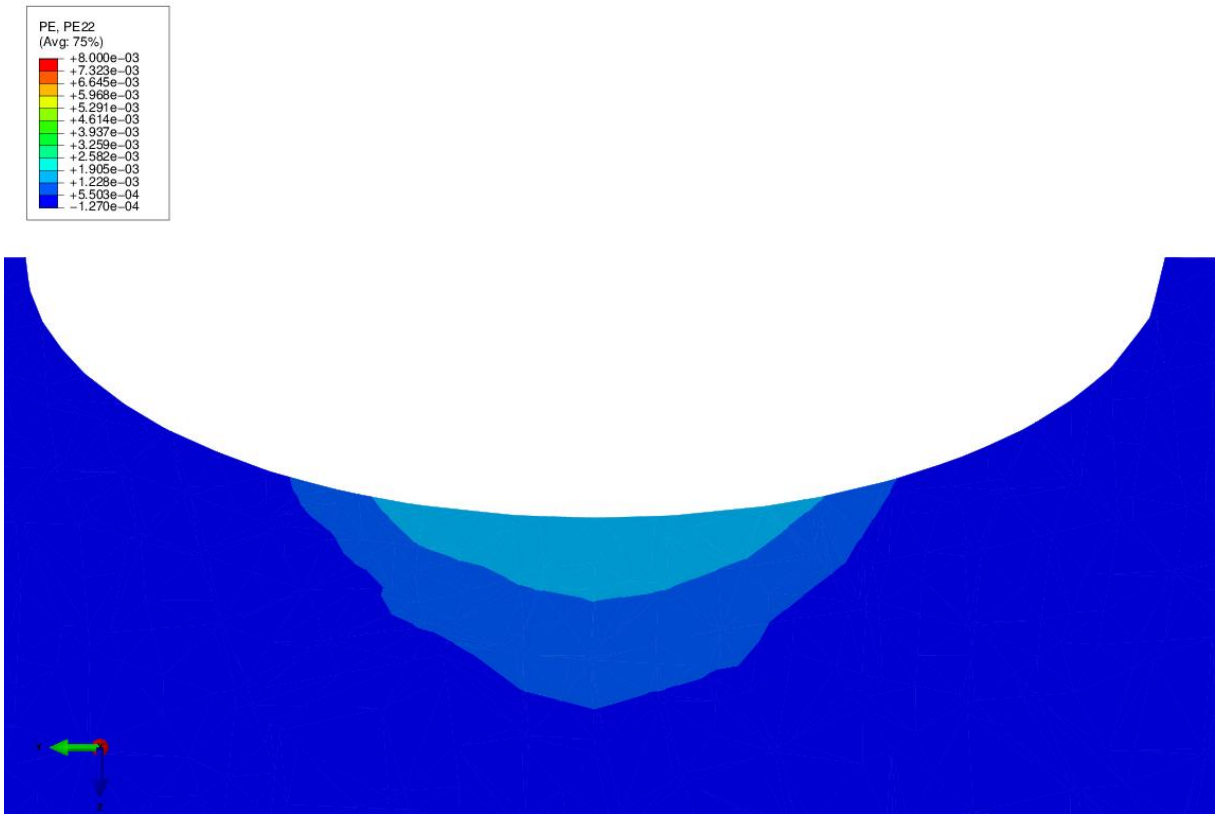

Figure 29: Cross-section of the smoothed version of the pit labelled 1800. The direction of loading is left to right. Note the change in colour coding from Figure 23.

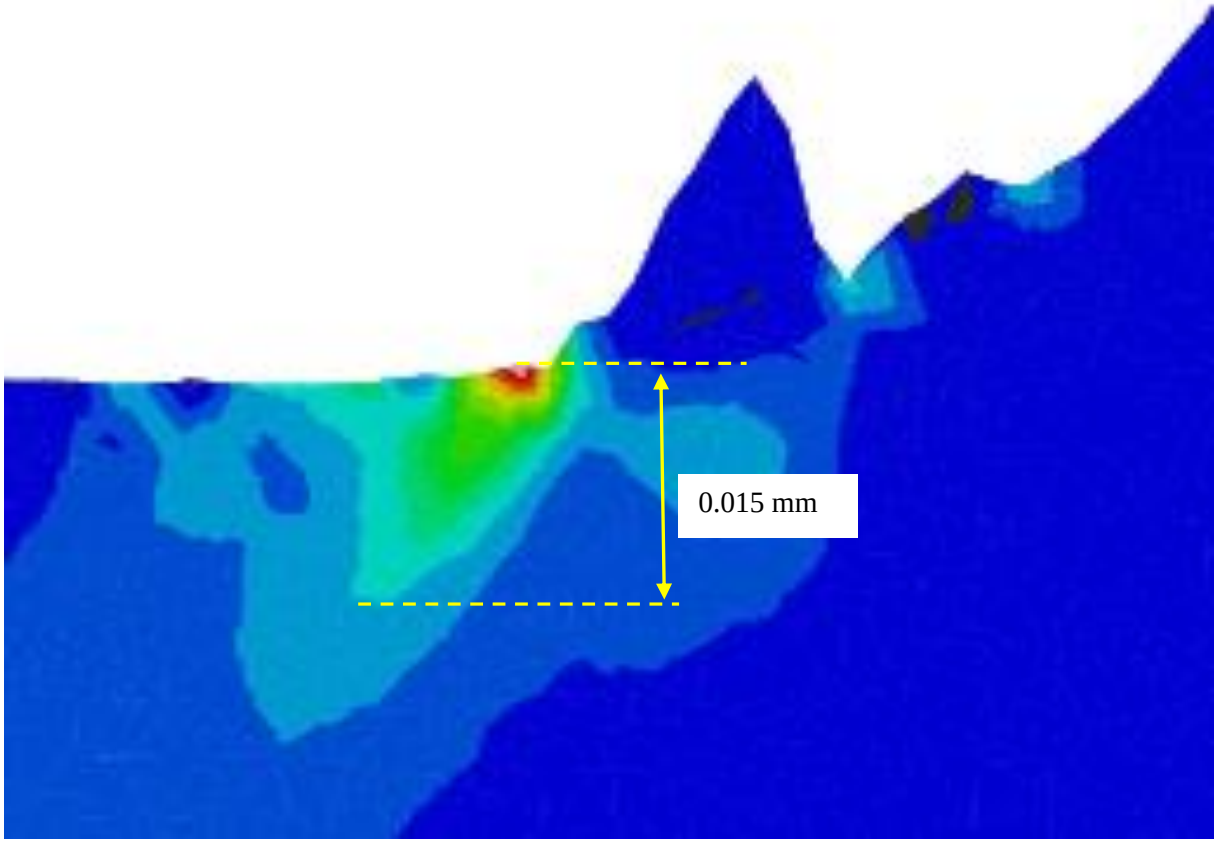

Figure 30: Close-up of feature in Figure 28: see Figure 28 for colour scale.

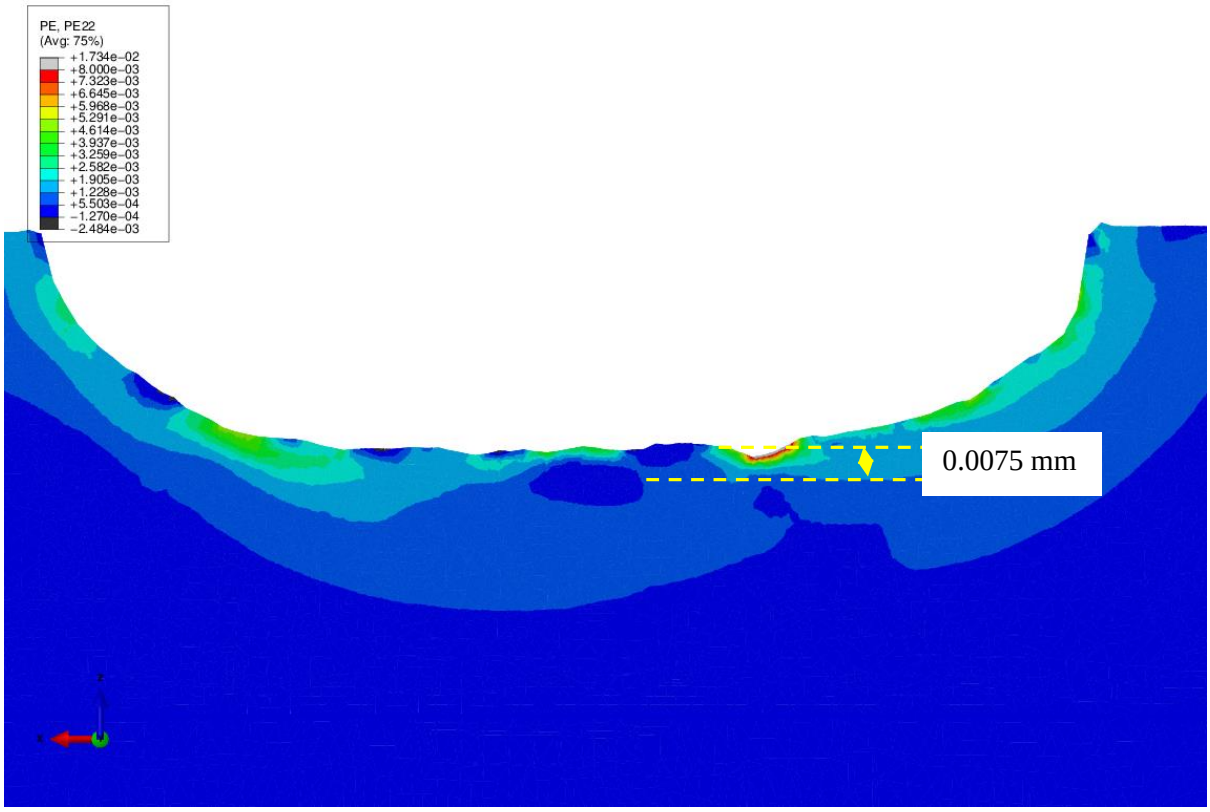

Figure 31: Cross-section of the lower of the circled figures in Figure 27. The direction of loading is into the page.

Figure 31 shows a similar cross-section through the lower of the circled regions in Figure 27.

It is apparent that in in most cases there is some degree of localised elevation of stress and strain, associated with troughs and also local to protrusions and for some pits a proliferation of such features. The plastic strain in these regions exceeds the values close to the pit mouth (cf. Figure 26 and 23). As raised in the Introduction to this report, a key question is the depth of material over which the localisation extends. While this will be material-environment dependent, the studies here indicate that significant plastic strain can exist to depths of 15 μm in some cases (note that most grains were generally smaller than 4 μm). In principle, these locations could then act as the preferred, or certainly additional, sites for initiation of a crack, albeit that there are factors other than stress and strain that will influence that process.

A limitation of this analysis is inability to account for the local microstructure. FE analysis considers the material to be homogenous. In practice, localisation of strain could arise also because of local variation in material properties at the grain size level and local variation in grain size. Hence, this FE analysis should only be considered indicative.

The extent to which embryonic cracks subsequently propagate can only be resolved through testing. In that context, there would be a virtue in characterising the pit topography prior to mechanical testing and interrupting the latter to establish the loci of crack initiation sites.

7 CONCLUSIONS

FE analysis of pits grown by a capillary methods on a C-steel indicate that plastic strain is a maximum close to the pit mouth and stress a maximum away from the mouth. This is similar to observations for hemispherical pits despite the very different geometry.

Variable topographical features were apparent from one pit to another intimating a possible source of inherent variability in corrosion fatigue crack initiation from pits. As expected, the adoption of an equivalent smooth pit gave results similar to the real pit when the latter were relatively free of significant features but could also be markedly different when these were significant.

Stress and strain localisation was apparent in relation to trough-like features in the pit but also adjacent to peaks in pit topography, which would suggest some shielding effect.

The depth below the surface for which these features would influence the local stress and strain will be dependent on the size of the defects but it was notably of the order of 15 μm even for the case of shielding.

It is recommended that characterisation of the artificial pit topography be undertaken prior to fatigue testing and the latter interrupted to relate the site/s of crack initiation to the detailed topographical features.

8 ACKNOWLEDGEMENTS

This work was undertaken in collaboration with MIT and UoM as part of a BP sponsored project in its Inherently Reliable Facilities flagship programme.

9 REFERENCES

[1] D. A. Horner, B. J. Connolly, S. Zhou, L. Crocker, A. Turnbull, “Novel images of the evolution of stress corrosion cracks from corrosion pits”, *Corros. Sci*., 53 (2011) 3466-3485.
[2] A. Turnbull, L. Wright, L. Crocker, “New insight into the pit-to-crack transition from finite element analysis of the stress and strain distribution around a corrosion pit”, *Corros. Sci.*, 52 (2010) 1492-1498.

[3] A. Turnbull, L. Crocker, “Finite element analysis of the effect of pit shape on the local stress and strain distribution”, NPL Report MAT 51, 2011.
[4] J.T. Burns, J.M. Larsen, R.P. Gangloff, “The effect of initiation feature on microstructure-scale crack propagation in Al-Zn-Mg-Cu”, *Int. J. Fatigue*. 42 (2012) 104-121.
[5] J. Ma, B. Zhang, J. Wang, G. Wang, E-H. Han, W. Ke, “Anisotropic 3D growth of corrosion pits initiated at MnS inclusions for A537 steel during corrosion fatigue”, *Corros. Sci*. 52 (2010) 2867–2877.
[6] R. Ballinger, Massachusetts Institute of Technology, Private communication, 2015.
[7] R. Leiva-garcia, University of Manchester, Private communication, 2015.